Modeling the Martian dust cycle 2. Multiannual radiatively active dust transport simulations

Journal Item

Modeling the Martian dust cycle. 2: Multi-annual radiatively active dust transport simulations

Claire E. Newman, Stephen R. Lewis, and Peter L. Read

Atmospheric, Oceanic and Planetary Physics, Department of Physics, Oxford University, Oxford, England

François Forget

Laboratoire de Météorologie Dynamique du CNRS, Université Paris 6, Paris

Abstract

Multi-annual dust transport simulations have been performed using a Mars general circulation model containing a dust transport scheme which responds to changes in the atmospheric state. If the dust transport is 'radiatively active' the atmospheric state also responds to changes in the dust distribution. This paper examines the suspended dust distribution obtained using different lifting parameterizations, including an analysis of dust storms produced spontaneously during these simulations. The lifting mechanisms selected are lifting by a) near-surface wind stress and b) convective vortices known as dust devils. Each mechanism is separated into two types of parameterization: threshold-sensitive and -insensitive. The latter produce largely unrealistic annual dust cycles and storms, and no significant interannual variability. The threshold-sensitive parameterizations produce more realistic annual and interannual behavior, as well as storms with similarities to observed events, thus providing insight into how real Martian dust storms may develop. Simulations for which dust devil lifting dominates are too dusty during northern summer. This suggests either that a removal mechanism (such as dust scavenging by water ice) reduces opacities at this time, or that dust devils are not the primary mechanism for storm production. Simulations for which near-surface wind stress lifting dominates produce the observed low opacities during northern spring/summer, yet appear unable to produce realistic global storms without storm decay being prevented by the occurrence of large-scale positive feedbacks on further lifting. Simulated dust levels are generally linked closely to the seasonal state of the atmosphere, and no simulation produces the observed amount of interannual variability.

1 Introduction

Studying and predicting the climate of Mars is made substantially more difficult by the large spatial and temporal variations in the atmospheric dust distribution, which has a significant radiative impact and hence affects greatly the atmospheric state. Atmospheric dustiness may vary considerably through a Martian year, and although there is a general annual trend

in dust loading there is also much interannual variability, most significantly in the number and size of dust storms which occur. In order to model the observed annual cycle of dust opacity on Mars, the observed range of dust storm types, and the interannual variability which occurs, a dust transport scheme (described in *Newman et al.* [2002], hereafter referred to as P1), has been added to a general circulation model of the Martian atmosphere (MGCM, see P1 and *Forget et al.* [1999]) to form a dust-transporting MGCM (DMGCM). The dust transport scheme is then able to respond to changes in the model's atmospheric state, which in turn is able to respond to changes in the transported dust distribution via the MGCM's radiation scheme if the transport is 'radiatively active'.

The aspect of dust transport which is currently most uncertain is dust lifting. Despite decades of observing Mars the spatial and temporal distribution of dust injection remains largely unknown. In P1, two mechanisms were selected and parameterized, the first being lifting by near-surface wind stress. P1 demonstrated that, using MGCM winds as representative of winds on Mars, saltation of larger, more easily moved sand particles is probably necessary to increase surface stresses sufficiently to lift dust. Two parameterizations were used to find the saltation flux, with the dust flux subsequently set proportional to this using a constant of proportionality α_N, the near-surface wind stress 'lifting efficiency'. The threshold-sensitive parameterization, NOG, calculates a saltation flux dependent on the amount by which drag velocities in the MGCM exceed thresholds for sand movement. The GST parameterization is similar, but also considers wind 'gustiness' (the probability distribution of wind speeds). This enables lifting to take place in areas where MGCM drag velocities (representative of the slowly-varying, background values which occur on Mars) are below threshold, so this parameterization is relatively threshold-insensitive.

The second mechanism, lifting by convective vortices known as dust devils, was also parameterized in two ways in P1. The threshold-sensitive parameterization, DTH, predicts the lifted dust mass per unit area by comparing tangential wind speeds around the vortices (estimated using the convective heat engine model of *Rennó et al.* [1998]) with thresholds for lifting based on laboratory experiments (*Greeley and Iversen* [1985]). The lifted dust flux is then found by multiplying by the dust devil 'lifting efficiency' α_D (which corresponds to a lifting rate for the DTH parameterization). The second parameterization, DDA, sets the lifted dust flux proportional to the 'dust devil activity' (a measure of how much energy may be harnessed to produce vortices, predicted by the heat engine model), with α_D the constant of proportionality. DDA is therefore threshold-insensitive, with lifting only ceasing when the dust devil activity reaches zero.

P1 showed that the near-surface wind stress lifting mechanism generally exhibits strong positive feedbacks, whereas the dust devil mechanism exhibits negative feedbacks. Initial predictions of dust lifting also suggested that the threshold-sensitive parameterizations, which require more extreme conditions to initiate dust lifting than the threshold-insensitive ones,

are less tied to the annual cycle and more linked to specific areas and/or times. This suggests that they will show more interannual variability than the threshold-insensitive versions if these extreme conditions do not occur every year. The threshold-insensitive versions, by contrast, will tend to give similar results provided the annual cycle is broadly maintained (which is very likely as it is controlled largely by the seasonal cycle in solar insolation).

The experiments presented below demonstrate that these hypotheses are borne out by the results of longer (multi-annual) simulations. In section 2 the two threshold-insensitive parameterizations, GST and DDA, are first used briefly before attention is turned in section 3 to the threshold-sensitive schemes, NOG and DTH, first alone then in combination. Sections 3.1 and 3.3 include comparisons between storms produced spontaneously in the simulations and similar observed events. Section 4 then presents some conclusions, and comments on the possibility of determining the main mechanism responsible for producing Martian dust storms and the observed dust cycle.

There are four main requirements for any simulation to be deemed 'realistic', based on the observed features of the Martian dust cycle (e.g. *Martin and Zurek* [1993], *Clancy et al.* [2000], *Smith et al.* [2001]). Firstly, zonally-averaged visible optical depths should range from $\sim$0.1 up to a maximum of $\sim$2–5, depending on the number and size of large dust storms in a given year. Secondly, peak dust loadings should occur during southern hemisphere summer, with minimum loadings during northern hemisphere spring/summer. Thirdly, large, distinct (i.e. rapid growth with at least some decay prior to another event) dust storms should be simulated between $L_s \sim 160^\circ$ and 330° in some years. Finally, there should be some variability in the location, time of occurrence and magnitude of these events between different years of a given simulation.

Each DMGCM simulation shown uses radiatively active dust transport, is begun at southern spring equinox ($L_s=180^\circ$) and follows a long, equilibrated MGCM simulation in which a prescribed 'low dust scenario' dust distribution is used in the radiation scheme (see P1 and *Lewis et al.* [1999]). The thermal infrared optical properties of the dust are derived from work to match simulated spectra with spectra observed by the Infrared Interferometer Spectrometer on the Mariner 9 spacecraft (*Toon et al.* [1977], *Forget* [1998]). The optical properties of dust at solar wavelengths are those derived by *Clancy and Lee* [1991] from Viking Orbiter Infrared Thermal Mapper (IRTM) emission-phase-function measurements. By using these properties, rather than those appropriate for the 2μm diameter dust particles assumed by the dust transport scheme, the radiation scheme responds more as if a realistic particle size distribution were being used. Dust lifting is entirely parameterized in each experiment, and an infinite surface dust source is assumed, although no dust is lifted from ice-covered surfaces. Raised dust is injected into the lowest model layer (centered at $\sim$5m) but is then transported rapidly up through the lower atmosphere by the vertical diffusion scheme described in P1.

In the following τ denotes visible dust optical depth at 0.67μm, and τ_{610} visible dust optical depth corrected to the 610Pa surface (i.e., $\tau_{610}=\frac{\tau\times 610}{\text{surface pressure}}$). This removes the topographic signal which often dominates dust opacity (with a greater dust column over low terrain such as the Hellas basin). $\tau^{9\mu\text{m}}$ is used to denote infrared dust optical depth, as determined for example by the Thermal Emission Spectrometer on the Mars Global Surveyor spacecraft, and $\tau_{610}^{9\mu\text{m}}$ to denote infrared dust optical depth corrected to the 610Pa surface.

2 Radiatively active dust transport with threshold-insensitive lifting.

2.1 GST lifting only.

Figure 1 shows zonally-averaged τ_{610} ($\bar{\tau}_{610}$) in six latitude bands for the first four years of simulation GST1 which uses GST (threshold-insensitive near-surface wind stress) lifting only. Thresholds are calculated using interparticle cohesion I_p=5$\times 10^{-7}$Nm$^{-1/2}$ and saltating particle diameter S_p=90μm. Gustiness is represented using the gustiness parameter κ (described in P1) =1.5, and α_N=5$\times 10^{-7}$m^{-1}. This value is chosen to produce realistic dust opacities, as are all the lifting efficiency (α_N or α_D) values used in these simulations. The main feature of this plot is the close repetition from year to year, quite unlike the sizable interannual variability observed (*Zurek and Martin* [1993]). No simulation using only GST lifting showed significant interannual variability, despite some lasting up to 10 years, with a variety of parameter values used which gave rise to opacities encompassing the observed range (e.g., α_N=1–10 $\times 10^{-7}$m^{-1} with I_p=5$\times 10^{-7}$Nm$^{-1/2}$, and similarly over a range of α_N values using I_p=0.5, 1 and 2 $\times 10^{-7}$Nm$^{-1/2}$).

Turning to the individual years of GST1 the observed annual dust cycle is broadly reproduced. Southern summer sees a peak in dust loading, greatest within a zonal collar (all longitudes) from ∼15°S – 50°S, with a minimum during northern summer and opacities within the observed range. But even so there are problems, most significantly the long time span of the dust peak. These simulated 'storms' have far greater durations than the longest, largest storms which have been observed (such as the huge 1971 storm, which lasted ∼69° of L_s). Furthermore, the storms' initial growth is less rapid than observed.

The entire dust cycle produced here by the GST parameterization is in fact tied too closely to the seasonal cycle of solar insolation for there to be either much interannual variability or very rapid storm growth and decay. This is a consequence of the lack of a threshold cut-off, meaning that dust lifting is merely reduced (rather than prevented) in relatively low wind stress regions. The peak in lifting therefore tends to occur where wind stresses averaged over an entire sol are highest, rather than, for example, in areas where there is a definite peak at one time of sol. With zero lifting below threshold the latter areas might represent

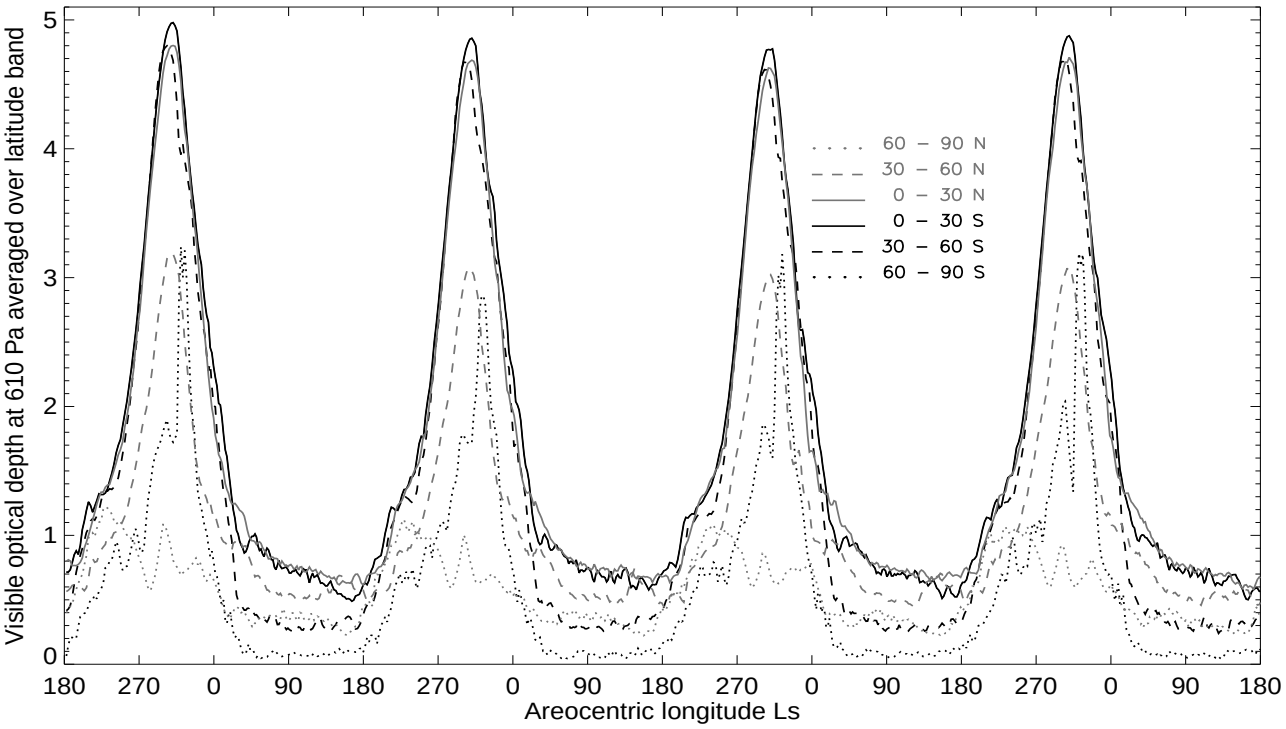

Figure 1: 4 years of zonally-averaged dust visible optical depths adjusted to the 610Pa surface ($\bar{\tau}_{610}$) for simulation GST1 (using GST lifting only with α_N=5×10^{-7}m^{-1} and I_p=5×10^{-7}Nm$^{-1/2}$). Results are shown for six latitude bands.

the only lifting on the planet, but using the GST parameterization they are of secondary importance. In general, owing to greater large-scale positive feedbacks, a simulation using GST lifting also results in a globally dustier and more homogeneous atmosphere than that simulated using NOG lifting (even if α_N has been tuned to inject initially the same amount of dust in both). This tends to increase the strength of the general circulation and shut down localized thermally-induced circulations. The net effect is the reduced importance of local strong wind regimes in favor of larger scale wind patterns. The atmospheric dust content becomes increasingly determined by the general circulation as the amount of dust rises (as it does during the storm season), and the smooth spatial and temporal variation of GST lifting is reflected in the generally smooth variation of atmospheric opacity through each year.

With positive feedbacks on further dust lifting, decay during the storm season is very unlikely with GST lifting. A 'stability' shut-down mechanism has been proposed by e.g. *Pollack et al.* [1979], in which the atmosphere becomes so stable due to increased dust lifting (and hence heating) that surface winds drop and further lifting ceases. This was not

found to occur in any simulations using the GST lifting parameterization, however, despite maximum zonally-averaged opacities greatly exceeding observed values (which are generally less than ∼5). With the GST parameterization the lifting is simply too evenly spread across the planet. In order for the stabilizing effects of airborne dust to become important in the DMGCM the dust lifting must be far more concentrated (such as in the NOG lifting results shown in section 3.1).

2.2 DDA lifting only.

Figure 2 shows $\bar{\tau}_{610}$ in six latitude bands for simulation DDA1 which uses DDA (threshold-insensitive dust devil) lifting only with α_D=1×10^{-8}kg J^{-1}. The results, especially during the dust storm season, are very similar to those using GST lifting only, although DDA1 also produces a peak in dust opacity during northern summer. This is because dust devil lifting is more directly linked to the annual cycle in solar insolation than is near-surface wind stress lifting. The latter is related via the more indirect effect of solar heating on circulation strength, which shows a greater intensity during southern summer than the relative solar insolation increase would suggest, due to other dynamical effects. This results in more near-surface wind stress lifting, and leads in turn to greater dust heating and a positive feedback between the circulation strength and dust lifting. For dust devil lifting the more direct link to the thermal forcing results in less seasonal asymmetry, and the negative feedbacks associated with increased dust levels act to reduce it further. The northern summer peak in DDA lifting is therefore quite large, about half the size of that in southern summer, rather than the latter dominating completely. The DDA1 opacity minimum is roughly a third of the peak value and is during northern spring, whereas the GST1 minimum is roughly an eighth of its peak value and is just prior to the start of the storm season in late northern summer.

2.3 Comments on threshold-insensitive lifting.

The annual cycle of dust opacity in simulations using the GST and DDA parameterizations of lifting has been found to be almost independent of the lifting efficiencies chosen. This is not true of the annual cycle of GST lifting, since an increasing proportion of storm season lifting occurs in the northern hemisphere as α_N increases (owing to stronger near-surface winds near the base of the descending branch of an intensified Hadley cell). The dust is, however, advected south across the equator by the Hadley cell at low altitudes, so still contributes more to southern than to northern opacities, and a similar latitudinal distribution of opacity to that shown in Fig. 1 is produced.

These results indicate that the threshold-insensitive parameterizations are unlikely to simulate realistic Martian dust cycles unaided. The lack of distinct storm events during the storm season suggests a need for some extra component to trigger storm decay during this

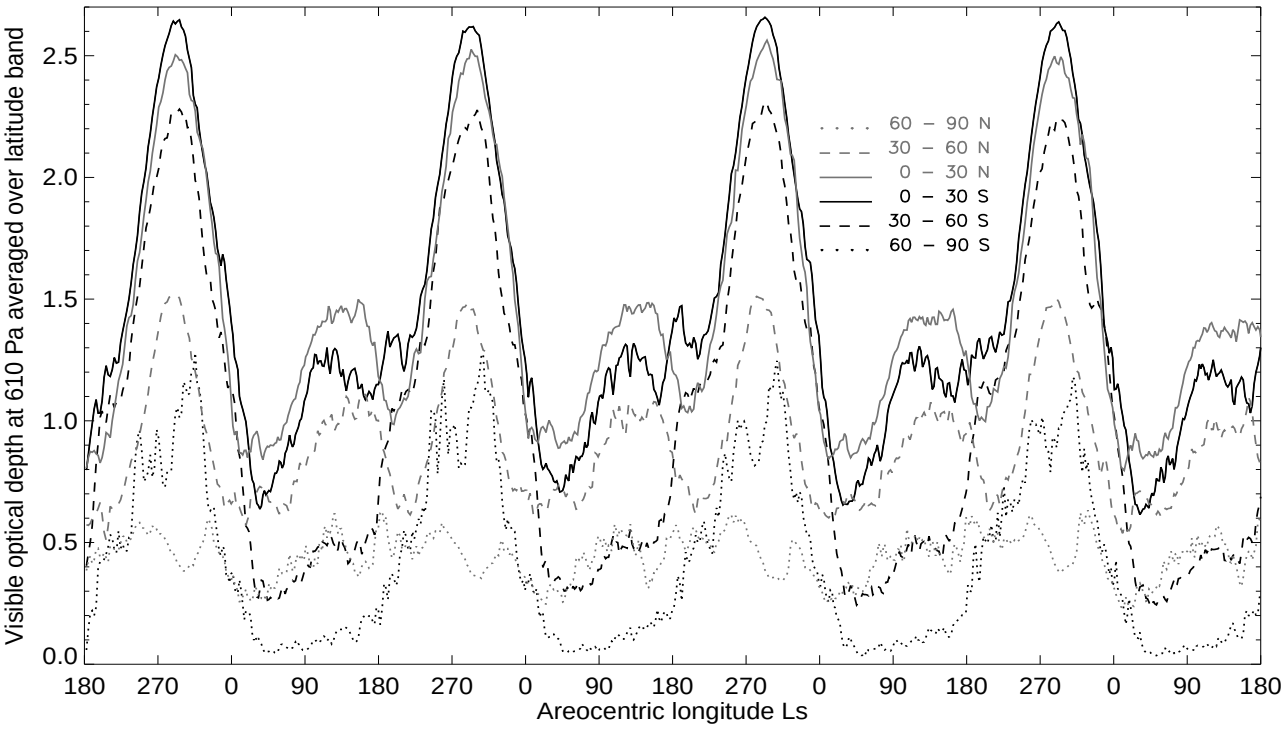

Figure 2: As in Fig. 1 but for simulation DDA1 (using DDA lifting only with α_D=1×10^{-8}kg J^{-1}).

period (in which the atmospheric state is such that peak lifting is predicted in the simulations shown above). One possibility is the use of a finite surface dust supply, the idea being that, if the dust supply is exhausted at the main lifting grid-points midway through the storm season, further lifting is reduced causing a decay in atmospheric dust opacity. As noted by e.g. *McKim* [1996], however, this is unlikely to explain the observation of storm seasons with two or more distinct storms which share onset regions (unless the dust is replenished between the decay of one storm and onset of the next).

Experiments conducted using the DMGCM appear to confirm this, with the depletion and resupply of dust being too gradual to account for observations. In a simulation begun with a finite surface dust source, and using only the GST lifting parameterization, for example, the first areas to be completely depleted are those with the greatest predicted lifting, leaving those with slightly less predicted still able to contribute for a while until they too are completely depleted, and so on. The reduction in dust injection is therefore gradual and smooth in terms of amount, and also in terms of location (since GST lifting generally varies smoothly from region to region). This gradual decrease in dust lifting throughout the storm season merely results in a more gradual rise in dust opacity to a reduced peak, and is not sharp enough to

mirror observed storm decay. A finite surface dust source also has the potential to increase interannual variability by changing the surface boundary condition present at the start of each year, but in the simulations described here the increased variability amounts to no more than a monotonic decrease in peak opacity from year to year.

3 Radiatively active dust transport with threshold-sensitive lifting.

3.1 NOG and background DDA lifting.

The relatively unpredictable nature of dust storms may be due largely to their onset mechanism(s) involving threshold processes, i.e., ones which require relatively unusual and extreme conditions to occur. Dust devils may be ubiquitous on Mars, occurring in almost every environment, as suggested for example by observations made by the Mars Orbiter Camera on Mars Global Surveyor (*Edgett and Malin* [2000]). It is therefore possible that low dust levels away from southern hemisphere summer are maintained by dust devil lifting, with the southern summer storms produced by bursts of threshold-sensitive near-surface wind stress lifting. The simulations shown in this section model such behavior by using DDA (threshold-insensitive dust devil) lifting to produce a small, background dust loading, and using NOG (threshold-sensitive near-surface wind stress) lifting to produce distinct storm events.

Although there are strong reasons for modifying surface winds to include gustiness effects (since MGCM winds will under-represent peak values, see P1 for further explanation), there are also valid reasons why the approach taken in the GST lifting parameterization may overestimate the amount of dust lifting. Firstly, it is unclear how much gustiness should be assumed, the choice of κ=1.5 being based on an analysis of Viking Lander data (see *Lorenz et al.* [1995,1996] and P1), which is available only at the two lander sites. Furthermore, the sampling was not suited to providing a κ value for wind speeds on sub-hourly timescales (although it was argued in P1 that the Viking Lander results give a lower limit to the amount of gustiness on smaller timescales). Secondly, the GST parameterization involves integrating the product of the probability density function assumed for drag velocity and an estimate of the horizontal sand flux (see P1), from the threshold drag velocity up to, effectively, infinity. There is consequently always a small contribution from integrating over the low probability (high wind-stress) tail of the distribution, even in regions with very low near-surface wind stresses. In reality there would be an upper limit on wind speed, and even below this the highest winds would not persist for long enough to induce and maintain a saltation flow capable of lifting dust.

In the following section the effects of threshold-sensitive dust lifting are shown by using the NOG parameterization, with gustiness removed altogether, which is probably too restricted

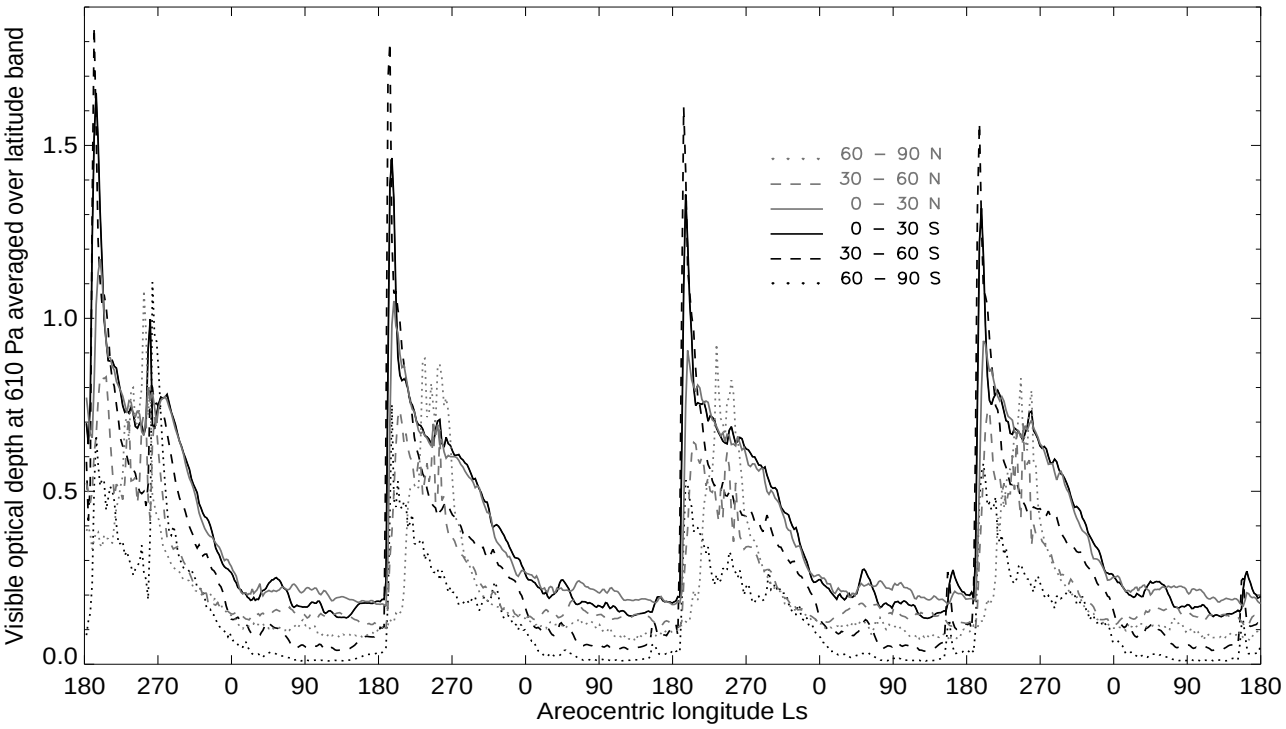

Figure 3: As in Fig. 1 but for simulation NOGDDA1 (using NOG and DDA lifting with α_N=5×10^{-5}m^{-1}, α_D=1×10^{-9}kg J^{-1} and I_p=5×10^{-7}Nm$^{-1/2}$).

towards the near-threshold situation. A more realistic parameterization might include a reduced upper limit of integration (corresponding to drag velocities having some moderate probability of occurrence). Sub-grid scale variations may also produce higher winds than those simulated at the resolution of the model, for example *Rafkin et al.* [2001] show that there is substantial enhancement of winds due to mesoscale topography.

3.1.1 Simulation NOGDDA1.

Figure 3 shows the evolution of $\bar{\tau}_{610}$ in six latitude bands for the first four years of an 11-year simulation, NOGDDA1. This uses a high value of I_p=5×10^{-7}Nm$^{-1/2}$, with S_p=90μm and α_N=5×10^{-5}m^{-1}, and has background dust devil lifting via the DDA parameterization with α_D=1×10^{-9}kg J^{-1}. The main feature of NOGDDA1 is the rapid growth of a dust storm shortly after southern spring equinox (peaking at L$_s$∼195°) corresponding to a large regional storm beginning in the Hellas region each year. This decays rapidly at first and, in three of the four years shown, decay then continues at a slower rate at all latitudes south of ∼45°N. In

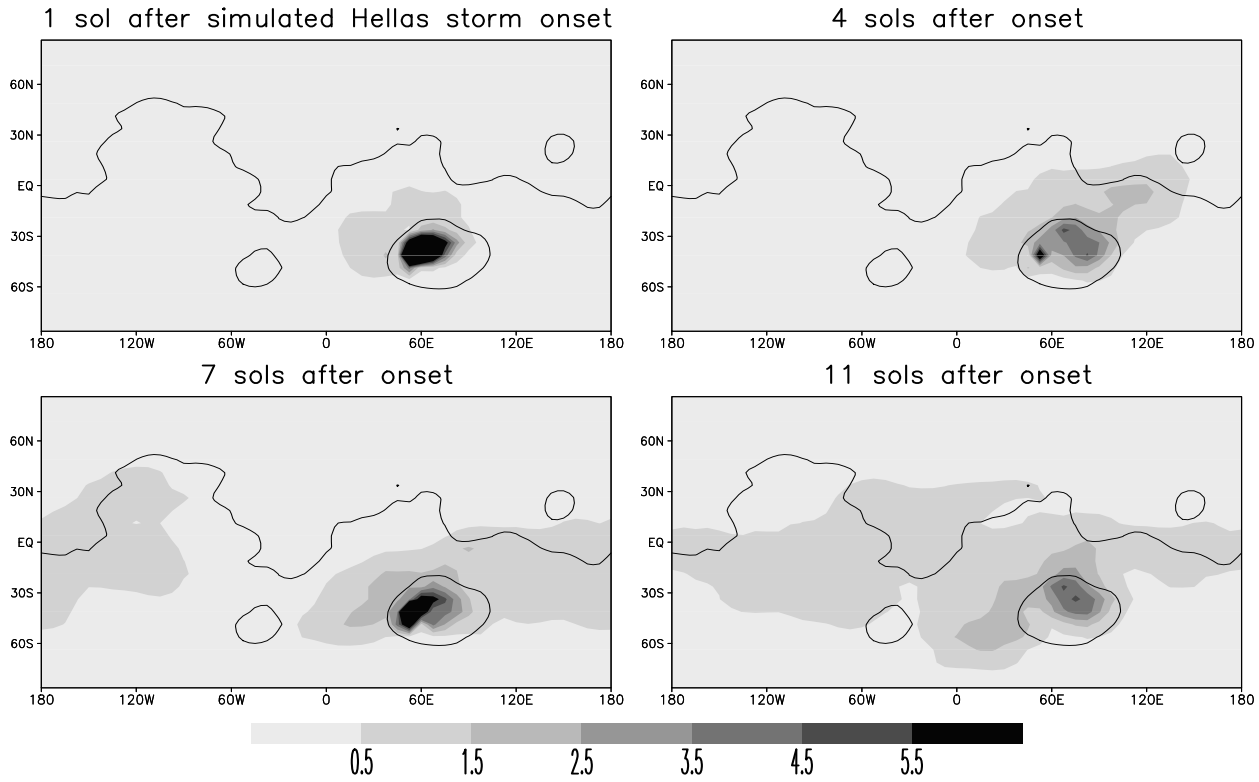

Figure 4: τ_{610} showing the development of the Hellas storm simulated in year 1. Onset is at $L_s \sim 186°$, and τ_{610} is shown at 4am at 0° longitude.

years 1 and 10, however, there is a secondary peak at $L_s \sim 255°$, which corresponds to a storm beginning north of the Chryse region and moving south within a western boundary current to the east of the Tharsis ridge (see e.g. *Joshi et al.* [1995] for a description of such flows on Mars). These Hellas and Chryse storms are discussed further in sections 3.1.3 and 3.1.4 respectively. Minimum opacities of ∼0–0.2 are reached by $L_s \sim 0°$, and persist until onset of the Hellas storm the following year.

3.1.2 Other simulations.

Experiments have also been performed to look at the effects of lower thresholds (by reducing interparticle cohesion). Simulation NOGDDA2 used a lower value of $I_p = 2 \times 10^{-7} \mathrm{Nm}^{-1/2}$, with $S_p = 75\mu\mathrm{m}$. $\alpha_N = 2 \times 10^{-5} \mathrm{m}^{-1}$ was chosen to produce approximately the same peak opacities as in NOGDDA1, and the same value of α_D was used as in NOGDDA1, producing similar

background dust devil lifting. NOGDDA2 also resulted in a large regional Hellas storm at $L_s \sim 195°$ each year, but the storms grew less rapidly owing to NOG lifting being less concentrated spatially and temporally in this lower threshold simulation, leading to reduced local positive feedbacks. Storm decay was also less dramatic, suggesting that in NOGDDA1, for which lifting is more restricted to a few grid points, the increased magnitude and homogeneity of dust opacity in such areas acts to enhance shut-down mechanisms (e.g., shut-down due to increased atmospheric stability or reduced horizontal temperature contrasts). NOGDDA2 also produced a second, broader peak centered on $L_s \sim 290°$ (shortly after summer solstice). This occurred because thresholds were low enough to be overcome by wind stresses produced at this time, and resembled the 'seasonally-controlled' peak found in simulations using the GST lifting parameterization, except that lifting was possible only near the northern base of the Hadley cell. By contrast, thresholds near the southern base remained higher than the strong westerlies present in that region, although advection in the north-south low level Hadley cell branch led to peak opacities centered south of the equator (from 45°S – 22.5°N).

Simulations with sufficiently low interparticle cohesions and/or sufficiently high α_D values all produced a broad peak centered shortly after summer solstice, in the former case because near-surface wind stress lifting thresholds were again exceeded during this period (as in NOGDDA2), and in the latter case because the southern summer dust devil lifting peak became substantial. As described in section 2, however, such an opacity peak is not representative of the rapidly growing storms observed on Mars itself. Simulation NOGDDA3 used $I_p = 1 \times 10^{-7} \mathrm{Nm}^{-1/2}$, $S_p = 58\mu\mathrm{m}$, $\alpha_N = 1.2 \times 10^{-5} \mathrm{m}^{-1}$ and $\alpha_D = 4 \times 10^{-9} \mathrm{kg\ J}^{-1}$ to produce dust opacity cycles which resembled those observed by Viking instruments in 1977, during which year two storms occurred during the storm season (see section 3.3.2). The main deficiencies of the simulation were an overly broad second opacity peak, little interannual variability and a lack of correspondence between the simulated and observed source regions. Peak dust opacities in the simulation were also slightly lower than those observed, although a north (winter) polar warming was simulated during the second storm, as observed in 1977. *Murphy* [1999] used a simple parameterization of near-surface wind stress lifting (using a constant threshold wind stress) and background prescribed dust devil lifting to also simulate dust cycles with two prominent maxima. His simulation produced narrower second peaks than NOGDDA3, but did not reproduce the observed north polar warming. Like NOGDDA3, it also failed to reproduce the observed source regions and lacked interannual variability.

3.1.3 The Hellas storm in simulation NOGDDA1.

This section examines the realism of the Hellas storms shown in Fig. 3 by analyzing the storm produced in year 1 of NOGDDA1. Figure 4 shows the evolution of τ_{610} for sols 1–11 after storm onset ($L_s \sim 186.5°$–$192.5°$). The storm begins when threshold drag velocities are exceeded over ice-free grid-points on the south-western slopes of Hellas. Here thresholds

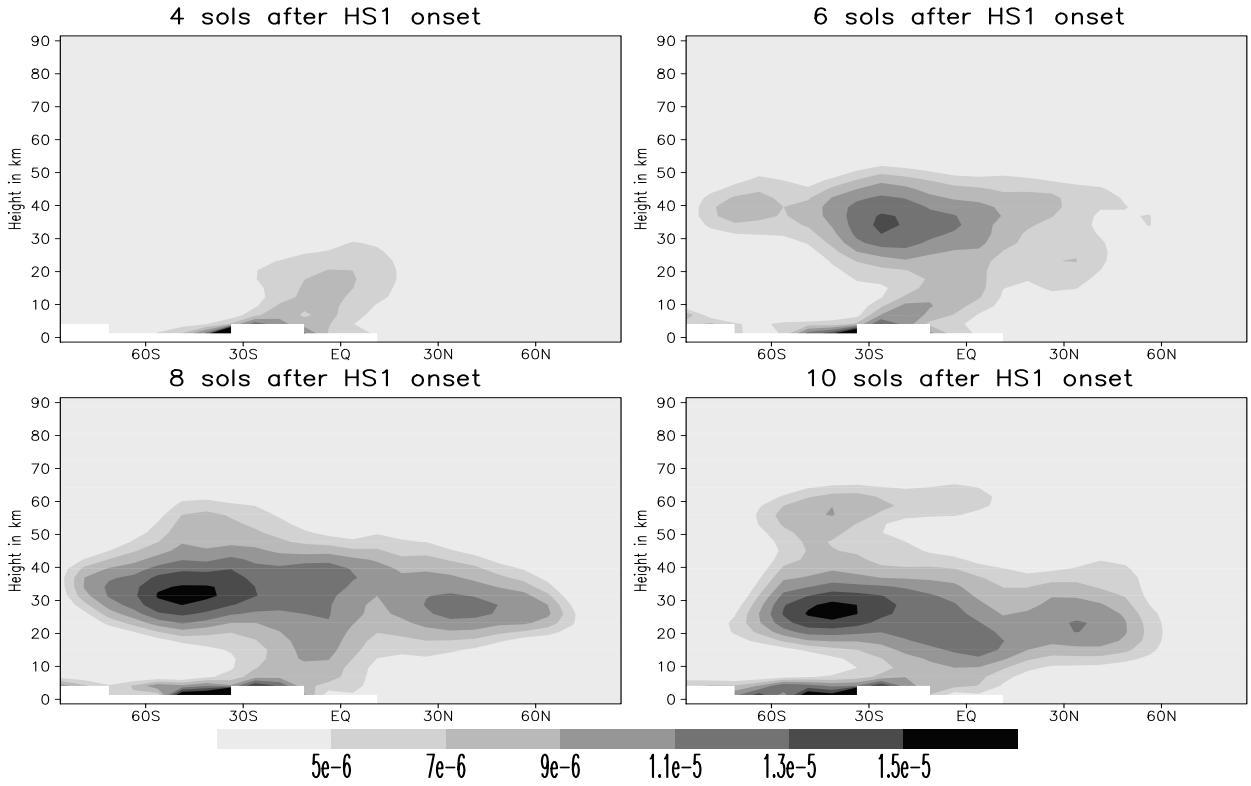

Figure 5: Zonally-averaged mixing ratios (kg/kg) showing the development of the Hellas storm simulated in year 1.

are particularly low due to the low temperatures found near the retreating (polewards and upslope) ice-cap edge, but drag velocities are high due to the seasonally intensifying large-scale circulation which is enhanced by strong local slope winds and thermal contrast flows. During the day, downslope winds over the ice-covered upper portion of the slope add to strong downslope winds caused by thermal contrasts at the ice-cap edge, to oppose upslope winds over the lower, ice-free portion of the slope. Towards nightfall these upslope winds decrease, but so do the ice-edge winds, hence a peak occurs at around 8pm local time (in qualitative agreement with two dimensional modeling work, *Siili et al.* [1999]). Storm onset in this simulation is therefore restricted to the period when the ice edge still covers part of the south-western slopes of Hellas, but has retreated sufficiently polewards that some grid-points where thresholds are exceeded are free of ice (and hence lifting is allowed).

Expansion occurs as additional grid-points are activated, due largely to positive feedbacks between the atmospheric state and dust lifting, with enhanced winds near the edge of the dust cloud. The main core has shifted eastwards and more directly over the basin after 4 sols, with dust carried away from Hellas to the north-east, extending into the Libya region. A secondary burst of lifting 3 sols after onset also results in dust beginning to be raised to higher levels after 4 sols, as shown in Fig. 5 which illustrates the vertical dust distribution during the storm's growth period. After 7 sols the lifting in the south-western corner of Hellas has increased again, with the storm spreading most readily to the west at $\sim$30°S then moving south west into Noachis. Some of the opacity increase over southern high latitudes at this time is due to upper level transport in a reverse cell (as illustrated by the upper right and lower two plots of Fig. 5) and is mechanically forced, mainly by thermal tides which are amplified due to the increased absorption of solar radiation by the increased dust column. Diurnal tide and stationary wave 1 amplitudes are increased over both north and south polar regions during the storm. Wave-forced polewards transport for a range of longitudes has also been noted in radiatively active dust transport simulations using other models (*Murphy et al.* [1995], *Wilson* [1997]), although these simulations used prescribed dust lifting and took place later during southern summer (near solstice).

Decay is triggered by increased thresholds in the source region as temperatures rise, with near-surface winds also reduced within the dust cloud as it becomes increasingly isothermal, and the storm has begun to dissipate by sol 11 without obscuring the south polar cap.

In the observational record (e.g. *Martin and Zurek* [1993], *McKim* [1999]) a number of storms match the general description of the simulated Hellas storm, especially a regional one observed in 1988 by several members of The Association of Lunar and Planetary Observers. It is described in *Beish et al.* [1989] as follows: "On May 5th. [$L_s \sim 189°$], during early Martian spring, one [a short-lived yellow cloud] appeared in the great Hellas basin. It expanded to the north for the next two days until it extended through Deltoton Sinus and into the Libya basin. A dull yellow haze pushed northwestward over Sabaeus Sinus and westward

into Noachis." After this point the storm rapidly dissipated. This corresponds relatively well with the simulated storm, the main difference being that it takes longer to dissipate and has more eastwards expansion than the observed event. In 2001 the complete lifecycle of a planet-encircling dust storm was observed by instruments on the Mars Global Surveyor spacecraft (see e.g. *Smith et al.* [2002]). The observed storm grew to become far larger than the Hellas storms found in simulation NOGDDA1, but was very similar in terms of the time ($L_s \sim 185°$) and location (Hellas) of its initial storm clouds.

3.1.4 The Chryse storm in simulation NOGDDA1.

As described above, a second type of storm appears in two years of the 11-year NOGDDA1 simulation, originating to the north of the Chryse region ($\sim$60°W, 30°N). Figure 6 uses τ_{610} to demonstrate the lifecycle of the Chryse storm simulated in year 1; the year 10 storm shows a very similar pattern of initiation and further growth. Both consist of initial storm clouds which form around the edge of the north polar cap, then are pulled out to the south west in a streamer which reaches into the northern Chryse region. Such clouds are largely a result of lifting by strong winds around northern Tharsis, and are common at this time of year in all years of the simulation, though only develop into large storms in years 1 and 10. A regional storm then develops over Chryse, and goes on to expand further as it moves south in the strong western boundary current to the east of the Tharsis ridge, with amplified lifting at the edge of the dust cloud due to the increased temperature gradients and hence increased wind speeds which occur there.

The enhanced winds at the storm's leading edge increase the already rapid western boundary current, resulting in a very fast-moving cloud heading towards the south pole, with little east-west expansion. For the year 1 storm, shown in Fig. 6, the amount of dust lifting begins to decrease in sol 5 when the cloud moves fully into the southern hemisphere, as even the enhanced drag velocities fall below lifting thresholds, and an increasing portion of the storm's evolution is due to the effects of transport rather than further lifting. As it nears the pole wind speeds drop and ice-covered regolith is encountered, preventing lifting altogether. By sol 10 it has begun to spread and dissipate over south polar regions, mainly within 60° of 0° longitude, and has almost completely decayed by sol 16.

The year 1 storm occurs at $L_s \sim 254°$, later in the storm season than that which occurs at $L_s \sim 236°$ in year 10, and, unlike the year 10 storm, produces a significant winter polar warming event. The two right-hand columns of Fig. 7 show that temperatures are elevated by 25K at $\sim$25 km above the north (winter) pole during the storm, compared with storm-free years. Other differences include a peak in temperatures at altitudes of $\sim$30 km over the south pole, and a cooler atmosphere above $\sim$70km (except in northern polar regions) during the Chryse storm. The two left-hand columns show the difference in zonally-averaged zonal winds with and without a late Chryse storm, and demonstrate the accompanying reduction

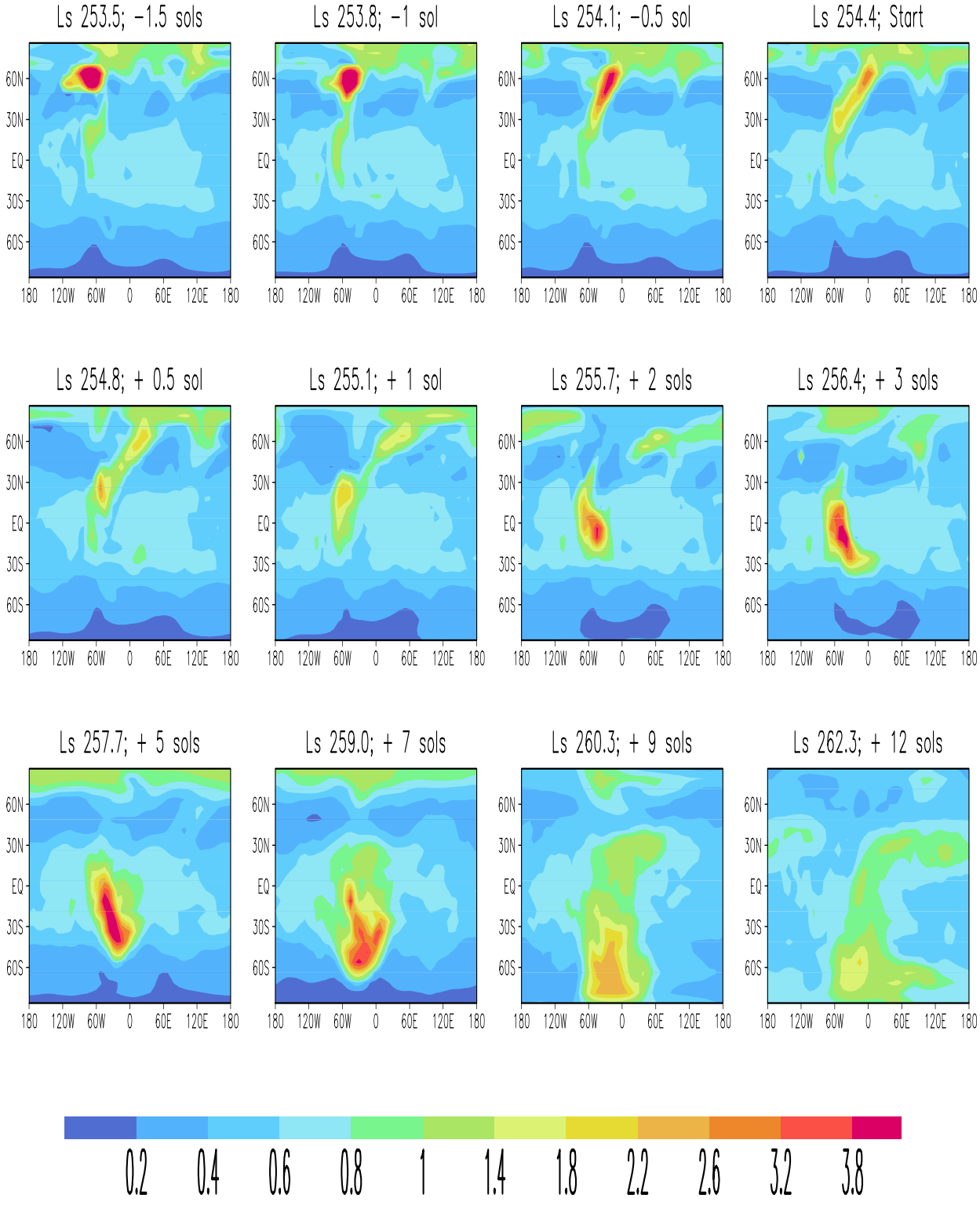

Figure 6: τ_{610} showing the growth of the Chryse dust storm simulated in year 1, from L_s=253.5° (1.5 sols before onset) until L_s=262.3° (12 sols after onset). The southwards movement is clearly visible.

in strength of the winter polar vortex and summer polar westerlies, and the large increase in strength of equatorial easterlies above $\sim$ 30km.

In 1999, Mars Global Surveyor instruments observed a regional storm at $L_s \sim 223°$, the development of which was strikingly similar to, in particular, the Chryse storm simulated in year 10. Mars Orbiter Camera observations (*Cantor et al.* [2001]) indicate that the observed storm also developed from local dust clouds around the north polar cap edge, and Thermal Emission Spectrometer maps of dust opacity (see e.g. Plate 2 of *Smith et al.* [2001]), although complicated by the presence of a second storm beginning soon after the Chryse storm, show a similar pattern of development in the Chryse region followed by southwards movement and growth. A detailed comparison between the observed and simulated storms, and an analysis of the onset, growth and decay mechanisms of the simulated Chryse storms, will be made in full in a subsequent paper.

3.2 DTH lifting only.

Having explored the effect of using the threshold-sensitive near-surface wind stress lifting parameterization, NOG, the next step is to use the threshold-sensitive dust devil lifting parameterization, DTH. Figure 8 shows 4 years of $\bar{\tau}_{610}$ for simulation DTH1, which uses only lifting by the DTH parameterization, with $\alpha_D = 1 \times 10^{-5} s^{-1}$. The most noticeable difference between DTH1 and previous simulations is the presence of sharp, distinct peaks at all times of year (largest within the storm season), which are far narrower than those produced using the DDA (threshold-insensitive dust devil lifting) parameterization. This is due to a combination of the negative feedback nature of dust devil lifting and the effect of localized, concentrated lifting events. Using DDA lifting, negative feedbacks in a radiatively active simulation gradually reduce the predicted dust lifting relative to that in an inactive simulation (as dust levels increase). This suggests that threshold-insensitive dust devil lifting is incapable of producing the rapid increase in dust levels observed during actual storm onset (see section 2.2). Using threshold-sensitive lifting, the situation is quite different, with this reduction of further lifting being less certain due to the fact that dust raising is far less spatially uniform.

Consider a region X in which a lot of dust is raised during a simulation using the DDA parameterization. The dust may be transported out of X to a neighboring region Y, but simultaneously dust from another neighboring region Z will be transported in. If dust lifting in X and Z are similar (as is likely for DDA lifting) then further lifting in X will still be reduced, even if all of the dust previously raised in X itself has been removed. But in the case of DTH lifting, if the large amount of dust lifted in area X is transported into Y, area Z may contain far less dust to be transported into X, leaving it relatively dust free, and hence providing conditions amenable to large amounts of further lifting. Eventually opacities may grow sufficiently over an area to cause a shut-down in dust devil lifting. At

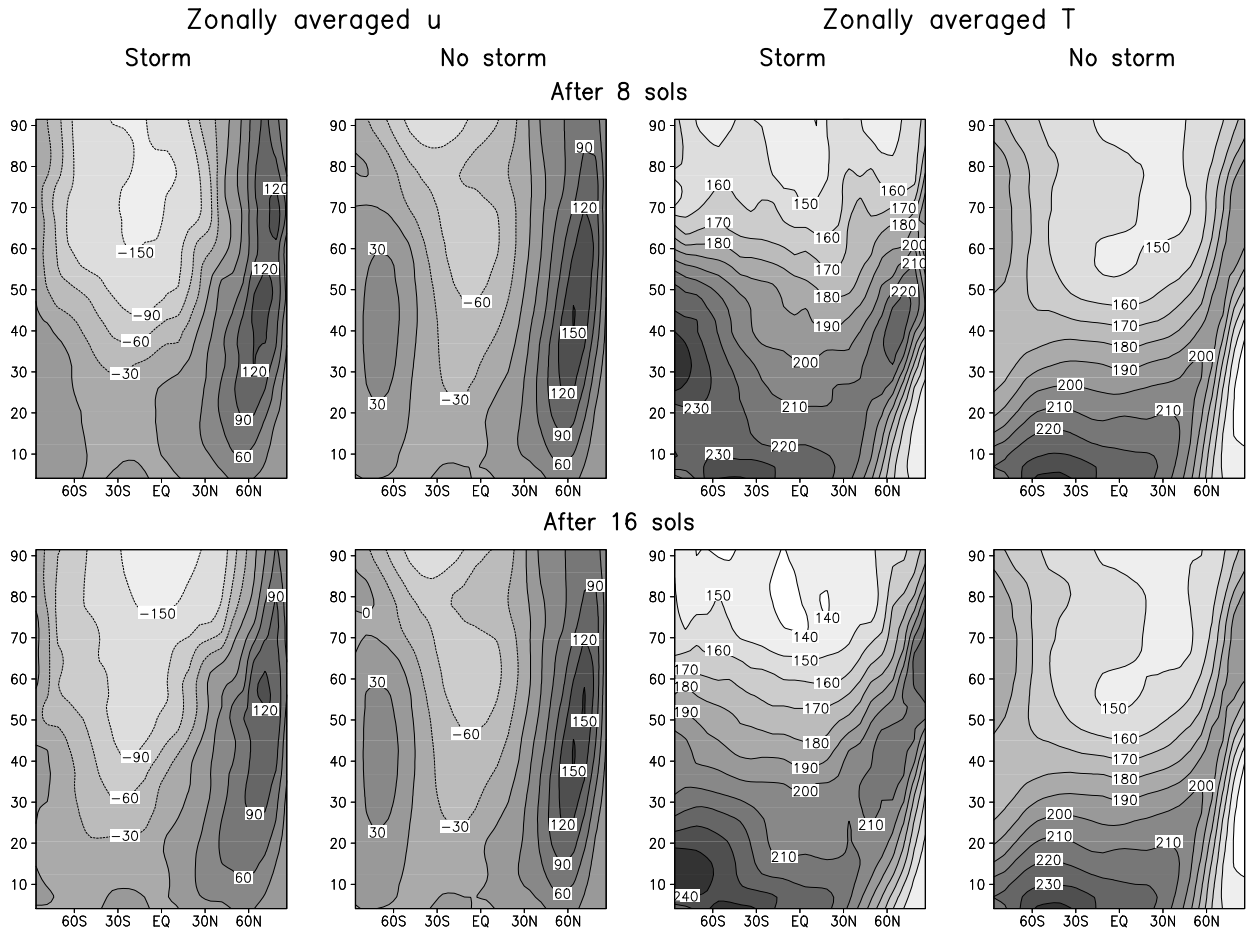

Figure 7: Simulated zonally-averaged zonal winds (left two columns) and temperatures (right two columns) in year 1 of NOGDDA1 (with a Chryse storm at $L_s \sim 255°$) and averaged over all years (2–9 and 11) without a Chryse storm. Times shown are sols after onset of the year 1 Chryse storm.

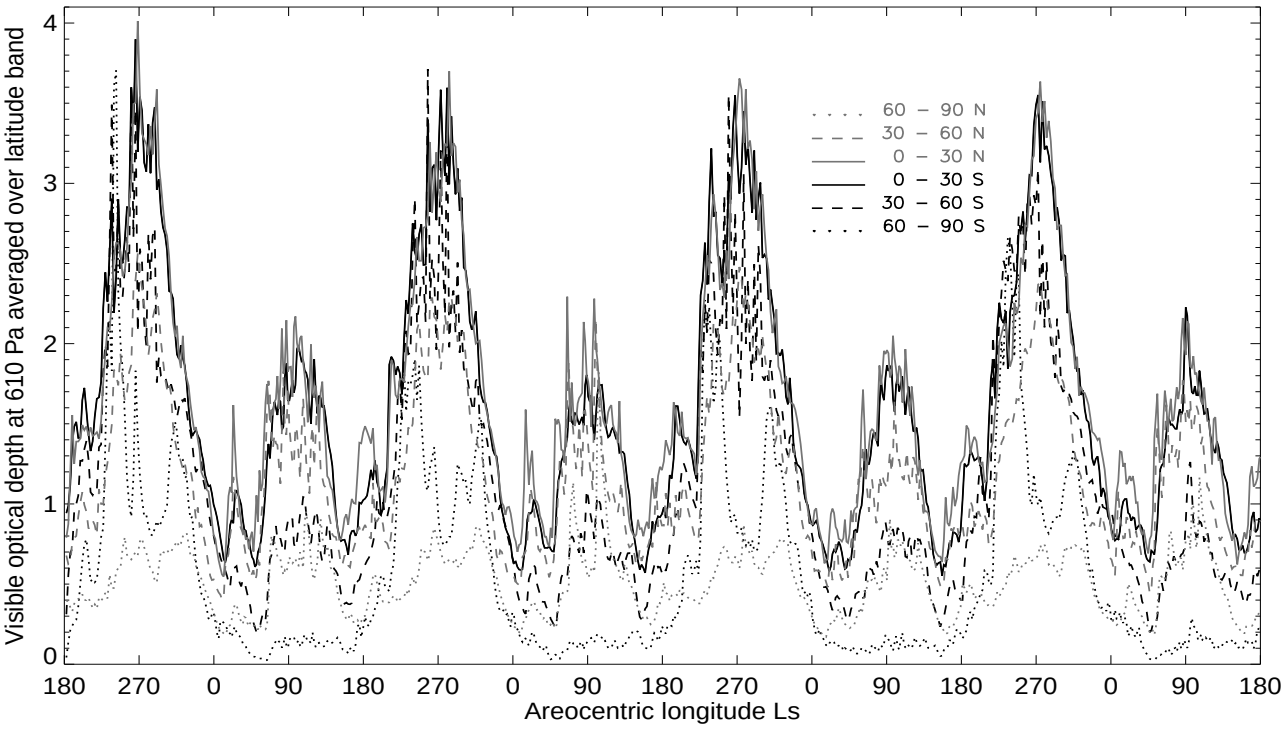

Figure 8: As in Fig. 1 but for simulation DTH1 (using DTH lifting only with α_D=1×10^{-5}s^{-1}).

the same time, however, other areas of the planet may be relatively dust free, allowing lifting there to continue, so there is a great potential for DTH lifting to alternate between regions, with strong lifting in one followed by shut-down, and the main lifting switching to another region while the first clears. Incidentally, NOG (threshold-sensitive near-surface wind stress) lifting also has negative feedbacks (e.g. the reduction of near-surface winds within opaque, isothermal dust clouds, particularly in regions where lifting is due to flows induced by temperature contrasts), yet does not show the behavior described above. This is because higher dust concentrations are generally required, to activate negative feedbacks, in simulations using the NOG parameterization than in those using the DTH parameterization, and they are also generally confined to areas of very strong localized lifting (e.g. the slopes of Hellas) rather than occurring over broad areas.

Simulations using the threshold-sensitive DTH lifting parameterization also show more interannual variability, in terms of the dust opacity cycle and storms produced, than the previous simulations presented. This stems from increased variability in the time and location of dust storms, further complicated by zonal variations in transport (with existing variations added to by those due to asymmetric dust heating). A large opacity peak occurs in year 1 in

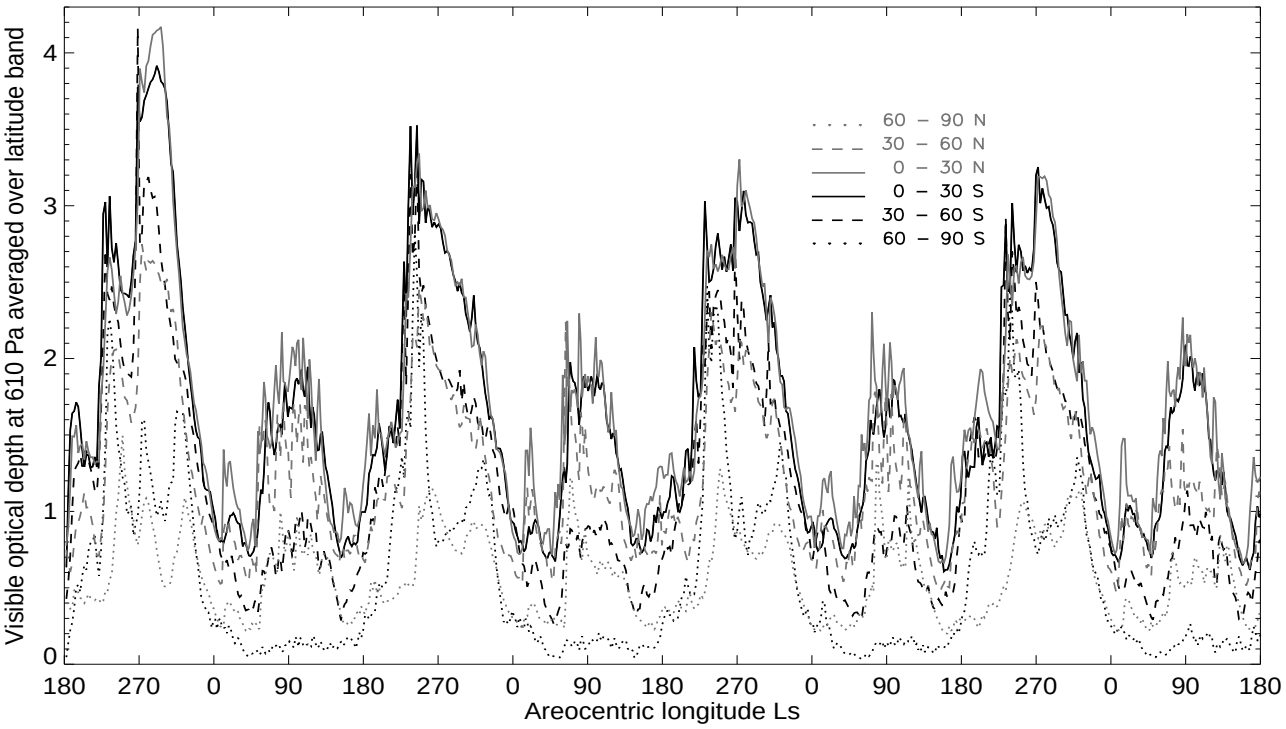

Figure 9: As in Fig. 1 but for NOGDTH1 (using NOG and DTH lifting with α_N=5×10^{-6}m^{-1}, I_p=1×10^{-7}Nm$^{-1/2}$ and α_D=1×10^{-5}s^{-1}).

the range 60°S–90°S, for example, and is greatly reduced in years 2–4, yet there is negligible lifting at these latitudes in any of the four years, which suggests that a variable transport mechanism causes the dust to spread more to polar regions in some years than in others. The growth and self-reduction of storms produced using the DTH parameterization, with peak lifting moving from region to region, gives rise to a greater variety of storms than found in previous simulations. The largest events tend to occur near 180°W and it is often these which spread to southern latitudes and obscure the south pole in simulations such as DTH1.

The same general pattern does, however, repeat from year to year, with peaks in northern mid-latitudes early in the storm season (L_s∼160°–210°) followed by peaks at low southern latitudes (L_s∼210°–240°) then in southern mid-latitudes (L_s∼220°–290°). There are also maxima in DTH lifting during northern hemisphere summer, as found using the DDA parameterization (section 2.2). The pattern of DTH lifting in radiatively inactive and active simulations is closely linked to areas with the largest convective boundary layer thicknesses (hence greatest thermodynamic efficiency), as described in P1. Their locations vary in radiatively active simulations, due to the complex interactions between solar insolation, spatial

variations in surface topography/thermal inertia, and the dust distribution, which determine the net heating response. Comparing the dominant lifting regions with those in simulations with NOG lifting only, the key difference is that peak lifting is no longer restricted to the Hellas basin and around northern topography. The Noachis region, which is almost a lifting minimum in results using the NOG parameterization, is one of three major lifting areas using the DTH parameterization: Noachis, the Hesperia/Mare Cimmerium region and Amazonis.

3.3 NOG and DTH lifting.

Despite uncertainty as to the relative importance of the near-surface wind stress and dust devil lifting mechanisms, several simulations have been performed using both the NOG and DTH lifting parameterizations, to explore the range of dust cycles possible if dust lifting on Mars is assumed to be threshold-sensitive.

3.3.1 Simulation NOGDTH1.

This uses NOG (threshold-sensitive near-surface wind stress) lifting with α_N=5×10^{-6}m^{-1} and I_p=1×10^{-7}Nm$^{-1/2}$, and DTH (threshold-sensitive dust devil) lifting with α_D=1×10^{-5}s^{-1}. Figure 9 shows the significant interannual variability in $\bar{\tau}_{610}$ produced as a result of this lifting combination. The contributions by NOG and DTH lifting during year 1 are shown in Figs. 10 and 11 respectively. Peak lifting by the NOG parameterization is about a quarter of that by the DTH parameterization in this simulation, and generally consists of lifting peaks in the latitude range 30°S–60°S during the first third of the storm season, in the range 45°S–45°N during the remainder, and with only a few smaller peaks, mostly in the range 30°S–60°S, during northern spring/summer.

Although its peaks are not quite as sharp as those for DTH lifting, NOG lifting evolves far less smoothly than in a simulation with NOG lifting only. DTH lifting is almost totally confined between 45°S and 45°N, with rapid increases followed by very rapid decreases (due to strong negative feedbacks), resulting in sharp peaks. The negative feedbacks on dust devil lifting (with increased dustiness reducing DTH lifting) are enhanced by the positive feedbacks on NOG lifting, since more NOG lifting, produced by greater dust amounts, causes opacities to increase still further, thus shutting down DTH lifting even more rapidly.

3.3.2 A 'Viking-like' storm season in NOGDTH1.

The evolution of dust opacity within the storm season in year 1 (and to a lesser extent years 3 and 4) bears a qualitative resemblance to that observed in 1977 during the Viking mission, with two global storms simulated at almost the same times of year as storms 1977a and b were observed by Viking instruments (*Martin* [1986]). Two global dust storms are simulated in

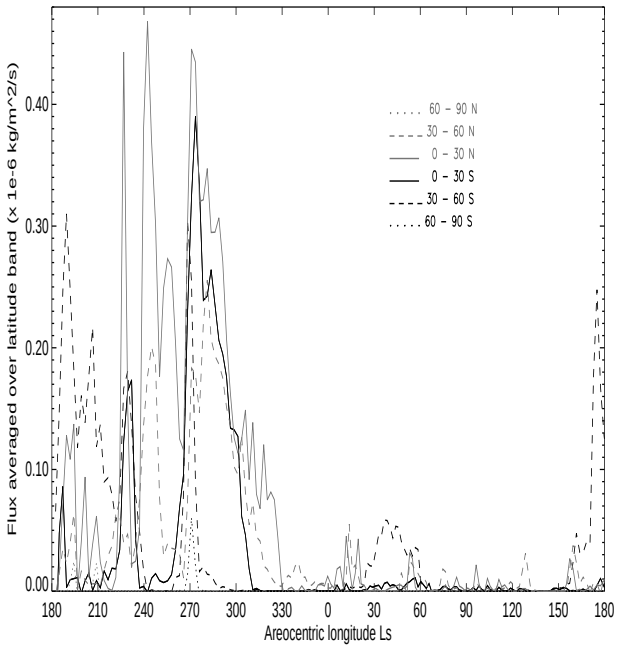

Figure 10: Zonally-averaged NOG lifting for year 1 of NOGDTH1, including storms A and B.

NOGDTH1, the first (storm A) beginning at $L_s \sim 219°$ and the second (storm B) at $L_s \sim 255°$, whereas 1977a began at $L_s \sim 204°$ and 1977b at $L_s \sim 268°$. Peak visible opacities of ~ 5 are similar to those observed by the Viking Lander instruments (*Zurek* [1981], *Colburn et al.* [1989]), with the second simulated storm larger than the first, also as in 1977. Continuing on into northern spring and summer, however, simulated opacities are far greater than observed (in any Mars year), mainly due to DTH lifting within the 0°–40°N latitude range.

An interesting question is: why are two distinct opacity peaks produced during the first storm season of NOGDTH1, with storm A decaying prior to storm B onset? The DTH parameterization has an important role to play, as its negative feedbacks provide a means of shutting down lifting during a period of peak solar insolation (which would result in peak lifting in a radiatively inactive simulation). The rapid opacity variations of simulation DTH1 (Fig. 8) reflect this, with the broader peaks of NOGDTH1 resulting from adding the NOG lifting parameterization. The most likely reason for storm A to decay is, as illustrated in Fig. 12, the increased planet-wide haziness produced during the storm's mature phase. This, most significantly, reduces the surface to air temperature difference over such a large area that DTH lifting cannot shift, as before, to a relatively dust-free region, since such regions no longer exist. NOG lifting is not sufficiently enhanced by the intensified circulation to compensate, and DTH lifting does not resume in strength until atmospheric opacities fall

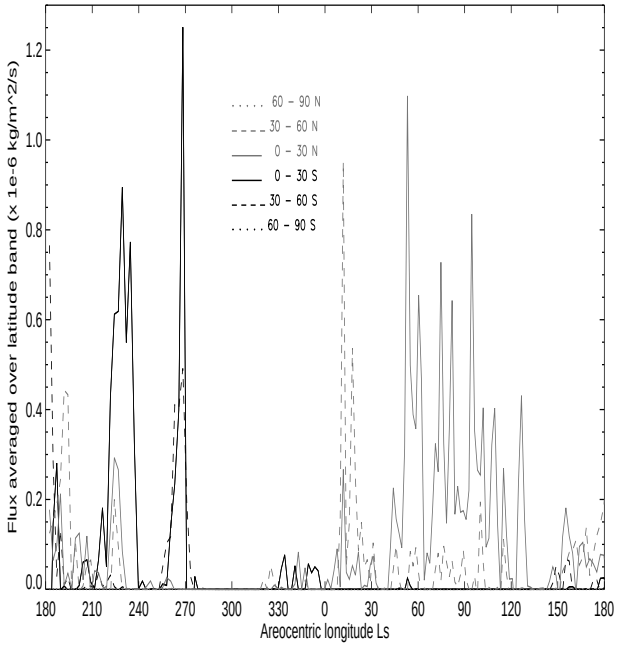

Figure 11: As in Fig. 10 but for DTH. Note the vertical scale in Fig. 10 shows a quarter the range used here.

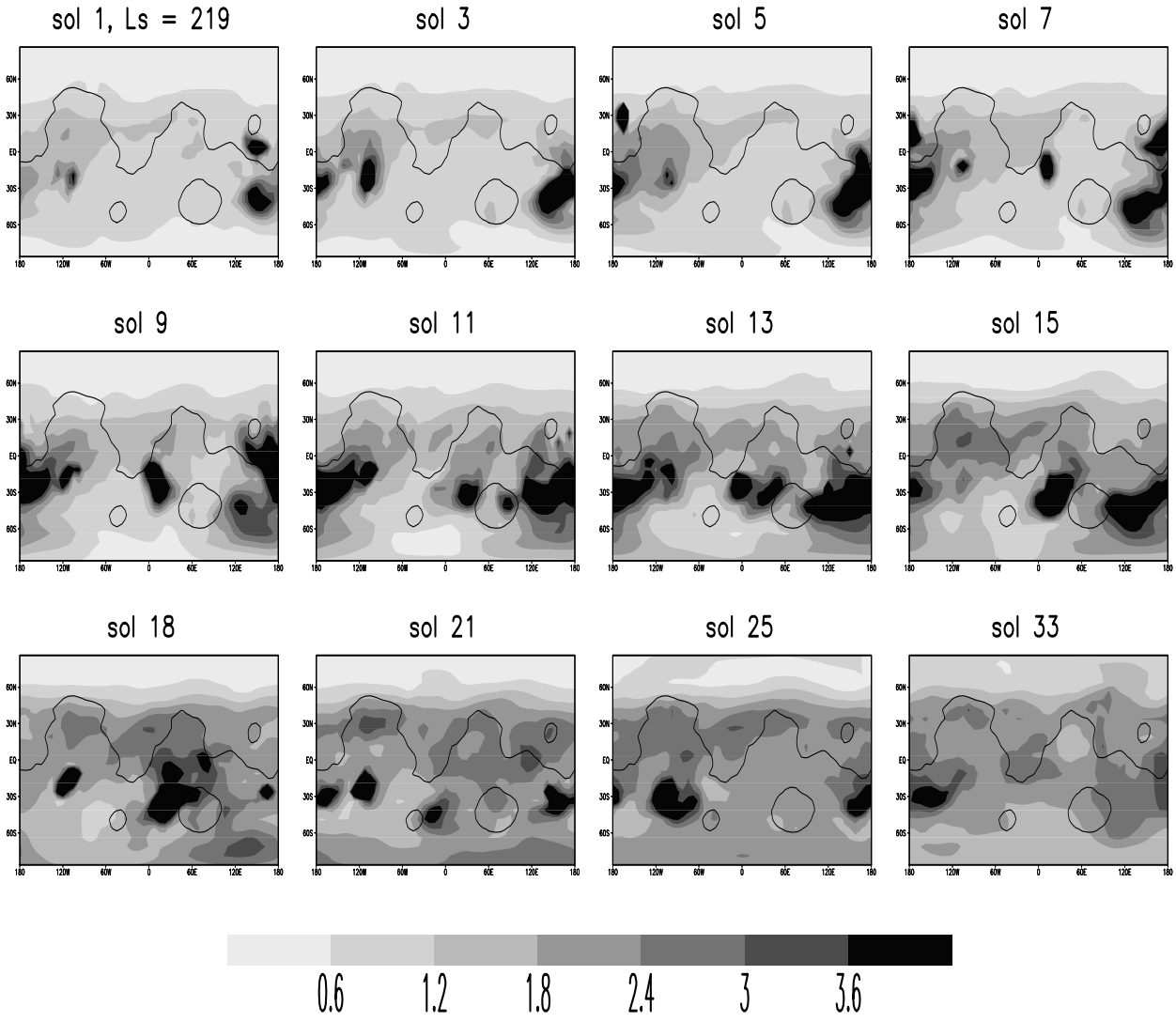

Figure 12: τ_{610} during storm A (the first storm of NOGDTH1) at the indicated number of sols after onset. The 575Pa surface pressure contour is shown in black to indicate the general positions of the Hellas and Argyre basins in the southern hemisphere.

over some areas of the planet. A dip in dust loading is therefore produced during the time of peak thermal forcing, due to the dust devil lifting mechanism's negative feedbacks, thus allowing two distinct global storms to occur in the same storm season. In the following year the pre-perihelic storm peak at $L_s \sim 230°$ (shown in Fig. 9) is larger than that for storm A, and the storm takes longer to decay. By the time that the atmosphere is clear enough for dust devil lifting to resume it is well past solstice, and the solar insolation available is apparently insufficient to produce the dust devil lifting required for a second storm peak.

The interplay between the two lifting parameterizations may be analyzed in more detail with reference to Figs. 10 and 11. As solar insolation increases towards perihelion, for example, DTH lifting peaks at $L_s \sim 228°$ in the range 0°–30°S (containing the latitudes which receive the greatest integrated insolation). Increased dust levels cause a positive feedback on near-surface wind stress, triggering increased NOG lifting which then causes DTH lifting to decline. As another example, peak DTH lifting during the height of southern summer is shut down abruptly at $L_s \sim 270°$ by the increase in dust loading, which, partly due to continued strong NOG injection until $L_s \sim 300°$, remains high until $L_s \sim 345°$ (well after the end of southern summer), preventing further peaks in DTH lifting for $L_s \sim 275°$–$320°$. The addition of NOG lifting modifies the DTH lifting behavior (rapid switching between regions) described in section 3.2. The variation in total lifting (and hence dust opacity) is 'buffered' by the presence of a second lifting mechanism which has the opposite reaction to changes in dust loading, hence the number of opacity peaks decreases.

Switching of peak lifting between different regions is found during the onset and expansion of the simulated storms A and B. The growth of storm A is illustrated in Fig. 12, which shows τ_{610} from $L_s \sim 219°$ (storm A onset) until $L_s \sim 240°$, 33 sols later. The storm is confined between 120°–180°E and 90°–180°W during the first 6 sols of growth, but in sol 7 a dust cloud appears north of the Noachis region in Sinus Sabaeus/Meridiani (∼20°E, 10°S), expanding southeast towards and into Hellas (initially relatively dust free) over the next few sols. The original storm center remains large, expanding south between ∼120°E and 180°E. By sol 18, however, opacities are reduced here, and the cloud dissipates over the south pole, raising polar visible opacities above 2 for the first time. Similar behavior continues until sol 33, by which time dust levels are decreasing over the south pole and most other regions, with a dust haze beginning to spread over north polar regions. Overall, storm A consists of at least 3 major storm centers, with a new center growing as an old one abruptly shuts down, and with some areas such as Solis/Thaumasia (∼100°W, 30°S) re-activating after dust levels have fallen.

The main difference between storms A and B is that the earlier storm A has dust clouds centered in general at lower latitudes than B, reflecting the more equatorwards position of the subsolar latitude (i.e., the location of greatest instantaneous heating) earlier in the storm season, prior to perihelion. Storm A in fact has similarities to a 1973 global dust storm (described in e.g. *Martin* [1976]), despite the latter beginning 80° later in L_s, which may be

due to the subsolar latitude being similarly placed at both times. Storm A also shows more changeability in the locations of the most active regions, and a greater ability to transport dust towards the south pole.

Storms A and B both show some similarities to the 1977a and b storms observed during the Viking mission. They develop at similar times of year, and share some common locations of early storm clouds: the Solis/Thaumasia region for storm A and 1977a (although storm A begins primarily in the Hesperia/Mare Cimmerium region) and near Argyre for storm B and 1977b (although in storm B the cloud is centered further east towards Noachis). In terms of expansion, storm A and 1977a both have strong activity in a broad, near-equatorial area centered at 140°E, but storm A also shows strong activity in Noachis/Meridiani and achieves far higher polar opacities than 1977a. In the southern hemisphere, storm B and 1977b are both more centered within a zonal collar from ∼15°S–45°S than the earlier storms, but storm B covers these latitudes less uniformly than the observed storm.

3.3.3 The atmospheric response during simulation NOGDTH1 compared to the Viking years.

The Viking IRTM instrument's 15μm channel provided representative temperatures ($T_{15\mu m}$) for a broad region of the atmosphere centered at ∼50Pa (*Martin and Kieffer* [1979]). Zonally-averaged simulated $T_{15\mu m}$ temperatures may be found, to a very good approximation, by convolving model temperature profiles with the IRTM channel's weighting function, and are shown in Fig. 13 for the first year of NOGDTH1. Observed values for a period including the 1977a and 1977b global dust storms are shown in Fig. 21 of *Wilson and Richardson* [2000] (where they are corrected for a radiance leak from the IRTM surface channel).

Figure 13 shows that simulation NOGDTH1 has a large warming over both poles during the storm season, peaking from L_s∼270°–300°, with temperatures of ∼220K in north polar regions, ∼200K over the pole itself (a warming of ∼50K), and just reaching 240K over the south pole. These temperatures slightly exceed (by less than 10K) those observed, but peak at the same time of year. Higher temperatures earlier in the year at southern high latitudes are also captured by the NOGDTH1 simulation, with no large northern hemisphere polar warming produced during storm A (in agreement with 1977a). Towards the end of the storm season, however, the simulation diverges significantly from observations, with temperatures ∼20K higher than those observed by L_s=0°.

A large, tidally-forced reverse cell, which is absent from MGCM standard dust scenario results for the same time of year, exists at southern mid to high latitudes during storm B in NOGDTH1. This increases the thermal drive to the Hadley cell, for example by increasing dust transport to southern high latitudes which results in greater radiative heating there, and produces a broader, more intense circulation. Examination of the residual mean circulation during storm B shows that the main Hadley cell extends further into, and is stronger in,

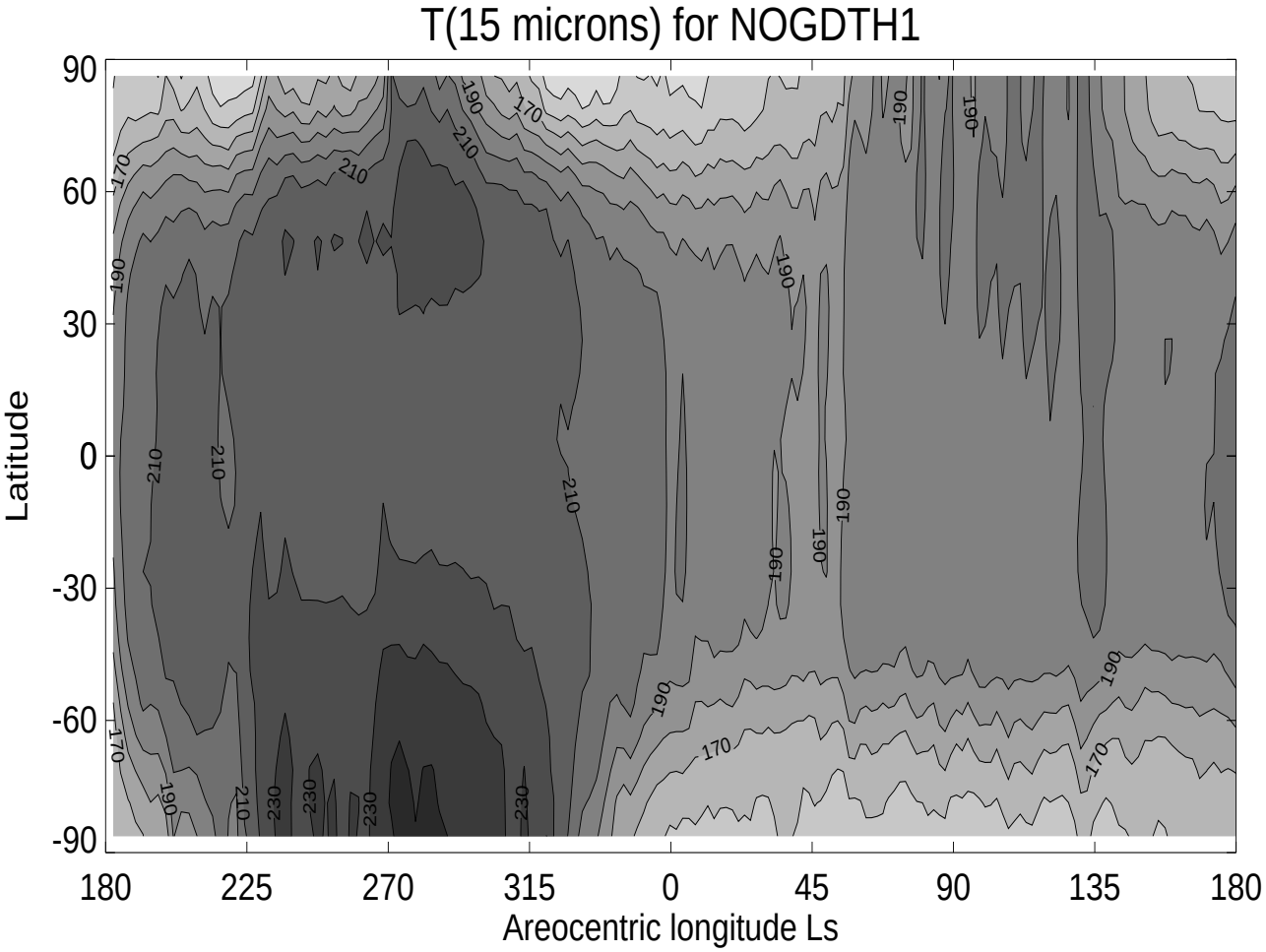

Figure 13: Zonally-averaged $T_{15\mu m}$ during the first year of simulation NOGDTH1.

northern polar regions. This increased downwelling, which is also closer to the pole than normal, enhances the adiabatic heating there and gives rise to a strong polar warming. *Wilson* [1997] used prescribed dust injection (into a Mars general circulation model with radiatively active dust transport) to model the polar warming observed during 1977b, and also found the tidal forcing of a reverse cell to be important in broadening the main circulation.

Simulated surface pressure tides have also been compared to those observed by the Viking Landers (e.g. *Zurek* [1981], *Wilson and Hamilton* [1996], *Wilson and Richardson* [1999]). Diurnal and semi-diurnal amplitudes are in quite good agreement during the storm season, but far too high during northern spring and summer in NOGDTH1. This may be attributed mainly to simulated dust opacities being too large during this period, and in fact amplitudes simulated during NOGDDA1 (with very low northern summer opacities) are far closer to those observed during the Viking mission. The observed reduction in tidal amplitudes between the two global storms, 1977a and 1977b, is also far less apparent between storms A and B, again probably owing to less clearing of the atmosphere between these two simulated storms than between the observed ones.

4 Conclusions

1. Stable, multi-annual simulations have been performed using the DMGCM with radiatively active dust transport and parameterized lifting, i.e., with a consistent atmospheric state, dust distribution and pattern of dust lifting at all times, without any resetting or adjustments required. The resulting atmospheric dust load does not increase from year to year, implying that a balance is rapidly achieved between the total amount of dust raised and the total amount removed. The interaction between dust transport and the atmospheric state allows feedbacks to occur, which enable quasi-realistic annual dust cycles to be produced. The dust storms which occur during these cycles are produced and shut down spontaneously by the model, and are determined by the lifting parameterizations selected. The model may therefore be used to investigate or identify mechanisms by which storms are initiated, grow and decay in the real atmosphere. Most of the parameters required by the lifting parameterizations are either unknown or poorly constrained, including the lifting efficiencies which are vital to determine the balance between near-surface wind stress and dust devil lifting. One method of determining which mechanism dominates and what lifting parameters are required is to consider which combinations produce simulated dust cycles, dust storms and interannual variability closest to those actually observed.

2. For lifting by both near-surface wind stress and dust devils, threshold-sensitive parameterizations provide the most realistic behavior, in terms of producing dust storms which grow rapidly and are capable of decaying prior to the decline in solar forcing which occurs towards the end of southern summer. If the primary lifting mechanism has little or no sensi-

tivity to thresholds an unrealistic dust cycle is produced, one which is too closely tied to the seasonal cycle, thereby producing each year an almost identical single, broad dust opacity peak encompassing southern spring and summer.

3. Simulation NOGDDA1, using the NOG (threshold-sensitive near-surface wind stress) and DDA (threshold-insensitive dust devil) lifting parameterizations, produces Hellas and Chryse storms with strong similarities to observed regional events in terms of onset times, onset regions and subsequent growth. Northern spring/summer opacities are low, consistent with observations, and the atmospheric response is also consistent with that during relatively clear years or periods.

No global dust storms are produced in NOGDDA1, however, or in any simulation using equally high near-surface wind stress lifting thresholds. Those using sufficiently high lifting efficiencies to raise dust levels over large areas, by means of positive feedbacks, eventually fail as dust levels increase too rapidly, owing to the same feedbacks required to produce a global storm in the first place. Work is underway to identify factors or processes which may limit this unstable growth, for example, using a finite initial surface dust source which may be entirely depleted in some regions during a simulation, or introducing scavenging of dust particles during water or CO_2 ice formation, both of which would serve to reduce the atmospheric dust content. Simulations using NOG and DDA lifting with reduced near-surface wind stress lifting thresholds (e.g. NOGDDA3) are able to produce larger dust opacity peaks, but these are too broad and do not grow sufficiently rapidly to resemble the global storms observed on Mars.

4. Simulation NOGDTH1, using the NOG and DTH (threshold-sensitive near-surface wind stress and dust devil) lifting parameterizations, produces a Viking-like storm season, with two opacity peaks at roughly the same times of year as storms 1977a and b. The simulated storms A and B have many similarities to those observed in terms of the areas of greatest storm activity, and the atmospheric response during the storm season is consistent with that observed, including the occurrence of a polar warming event during the second storm.

During northern spring and summer, however, dust opacities are far greater than observed, and the atmospheric response also diverges from that recorded. The elevated opacities are a fairly robust feature of all simulations in which dust devil lifting dominates, and are therefore unlikely to be reduced by varying details of the parameterization used. This suggests that dust devil lifting cannot be the major contributor to dust storms, which would be in agreement with the lack of correlation between observations of dust devils and the locations of initial storm clouds (*Cantor et al.* [2002]). Further work is required, however, to investigate the possible reduction of opacity during the clear seasons by, for example, water vapor scavenging.

5. Despite the variable appearance of a Chryse storm in NOGDDA1 and some interan-

nual variability in NOGDTH1, neither reproduces the large observed interannual variability, such as a clear year followed by a year with a planet-encircling dust storm. This may be partly due to the lack of interaction between the dust, CO_2 and water cycles. A finite surface dust source might also allow dust to be entirely depleted at times from certain regions, as dictated by the balance between lifting and sedimentation there, effectively resetting the boundary conditions each year. It is possible, however, that the lack of simulated interannual variability is due to the underrepresentation of feedbacks on local (down to sub-grid) scales, a theory which may be difficult to test in a global circulation model.

Acknowledgments

CEN and SRL gratefully acknowledge support for this work from the UK Particle Physics and Astronomy Research Council.

References

[1] Beish, J. D., D. C. Parker, and C. E. Hernandez, The red planet shows off, *Sky Teles.*, *77*, 30–35, 1989.

[2] Cantor, B., P. B. James, M. Caplinger, and M. J. Wolff, Martian dust storms: 1999 Mars Orbiter Camera observations, *J. Geophys. Res.*, *106*, 23653–23687, 2001.

[3] Cantor, B., M. Malin, and K. S. Edgett, Multiyear Mars Orbiter Camera (MOC) observations of repeated Martian weather phenomena during the northern summer season, *J. Geophys. Res.*, *107*, 3–1–3–8, 2002.

[4] Clancy, R. T., and S. W. Lee, A new look at dust and clouds in the Mars atmosphere: analysis of emission-phase-function sequences from global Viking IRTM observations, *Icarus*, *93*, 135–158, 1991.

[5] Clancy, R. T., B. J. Sandor, M. J. Wolff, P. R. Christensen, M. D. Smith, J. C. Pearl, B. J. Conrath, and R. J. Wilson, An intercomparison of ground-based millimeter, MGS TES, and Viking atmospheric temperature measurements: Seasonal and interannual variability of temperatures and dust loading in the global Mars atmosphere, *J. Geophys. Res.*, *105*, 9553–9571, 2000.

[6] Colburn, D., J. Pollack, and R. Haberle, Diurnal variations in optical depth at Mars, *Icarus*, *79*, 159–189, 1989.

[7] Edgett, K. S., and M. C. Malin, Martian dust raising and surface albedo controls: Thin, dark (and sometimes bright) streaks and dust devils in MGS MOC high resolution images, 2000, conference paper (Lunar and Planetary Science, XXXI).

[8] Forget, F., Improved optical properties of the Martian atmospheric dust for radiative transfer calculations in the infrared, *Geophys. Res. Lett.*, *25*, 1105–1109, 1998.

[9] Forget, F., F. Hourdin, F. Fournier, C. Hourdin, O. Talagrand, M. Collins, S. R. Lewis, P. L. Read, and J.-P. Huot, Improved general circulation models of the Martian atmosphere from the surface to above 80 km, *J. Geophys. Res.*, *104*, 24,155–24,175, 1999.

[10] Greeley, R., and J. D. Iversen, *Wind as a Geological Process on Earth, Mars, Venus, and Titan*, Cambridge University Press, 1985.

[11] Joshi, M. M., S. R. Lewis, P. L. Read, and D. C. Catling, Western boundary currents in the Martian atmosphere: Numerical simulations and observational evidence, *J. Geophys. Res.*, *100*, 5485–5500, 1995.

[12] Lewis, S. R., M. Collins, P. L. Read, F. Forget, F. Hourdin, F. Fournier, C. Hourdin, O. Talagrand, and J.-P. Huot, A climate database for Mars, *J. Geophys. Res.*, *104*, 24,177–24,194, 1999.

[13] Lorenz, R. D., J. I. Lunine, J. A. Grier, and M. A. Fisher, Prediction of aeolian features on planets: Application to Titan paleoclimatology, *J. Geophys. Res.*, *100*, 26,377–26,386, 1995.

[14] Lorenz, R. D., J. I. Lunine, J. A. Grier, and M. A. Fisher, Martian surface wind speeds described by the Weibull distribution, *J. Spacecraft*, *33*, 754–756, 1996.

[15] Martin, L. J., 1973 dust storm on Mars: Maps from hourly photographs, *Icarus*, *29*, 363–380, 1976.

[16] Martin, L. J., and R. W. Zurek, An analysis of the history of dust activity on Mars, *J. Geophys. Res.*, *98*, 3221–3246, 1993.

[17] Martin, T. Z., Thermal infrared opacity of the Mars atmosphere, *Icarus*, *66*, 2–21, 1986.

[18] Martin, T. Z., and H. H. Kieffer, Thermal infrared properties of the Martian atmosphere. 2. The 15μm band measurements, *J. Geophys. Res.*, *84*, 2843–2852, 1979.

[19] McKim, R. J., The dust storms of Mars, *J. Br. Astron. Assoc.*, *106*, 185–200, 1996.

[20] McKim, R. J., Telescopic Martian dust storms: a narrative and catalogue, in *Memoirs of the British Astronomical Association*, vol. 44, British Astronomical Association, 1999.

[21] Murphy, J. R., The Martian atmospheric dust cycle: Insights from numerical model simulations, 1999, conference paper (The Fifth International Conference on Mars).

[22] Murphy, J. R., J. B. Pollack, R. M. Haberle, C. B. Leovy, O. B. Toon, and J. Schaeffer, 3-dimensional numerical simulation of Martian global dust storms, *J. Geophys. Res.*, *100*, 26,357–26,376, 1995.

[23] Newman, C. E., S. R. Lewis, P. L. Read, and F. Forget, Modeling the dust cycle in a Mars general circulation model. 1: Representations of dust transport processes, *J. Geophys. Res.*, 2002, this issue.

[24] Pollack, J. B., D. S. Colburn, F. M. Flasar, R. Kahn, C. E. Carlston, and D. C. Pidek, Properties and effects of dust particles suspended in the Martian atmosphere, *J. Geophys. Res.*, *84*, 2929–2945, 1979.

[25] Rafkin, S. C. R., R. M. Haberle, and T. I. Michaels, The Mars regional atmospheric modeling system: Model description and selected simulations, *Icarus*, *151*, 228–256, 2001.

[26] Rennó, N. O., M. L. Burkett, and M. P. Larkin, A simple thermodynamical theory for Dust Devils, *J. Atmos. Sci.*, *55*, 3244–3252, 1998.

[27] Siili, T., R. M. Haberle, J. R. Murphy, and H. Savijärvi, Modelling of the combined late-winter ice cap edge and slope winds in Mars' Hellas and Argyre regions, *Plan. Space Sci.*, *47*, 951–970, 1999.

[28] Smith, M. D., J. C. Pearl, B. J. Conrath, and P. R. Christensen, Thermal Emission Spectrometer results: Atmospheric thermal structure and aerosol distribution, *J. Geophys. Res.*, *106*, 23,929–23,946, 2001.

[29] Smith, M. D., B. J. Conrath, J. C. Pearl, and P. R. Christensen, Note: Thermal Emission Spectrometer observations of Martian planet-encircling dust storm 2001A, *Icarus*, *157*, 259–263, 2002.

[30] Toon, O. B., J. B. Pollack, and C. Sagan, Physical properties of the particles comprising the Martian dust storm of 1971-1972, *Icarus*, *30*, 663–696, 1977.

[31] Wilson, R. J., A general circulation model simulation of the Martian polar warming, *Geophys. Res. Lett.*, *24*, 123–126, 1997.

[32] Wilson, R. J., and K. Hamilton, Comprehensive model simulation of thermal tides in the Martian atmosphere, *J. Atmos. Sci.*, *53*, 1290–1326, 1996.

[33] Wilson, R. J., and M. I. Richardson, Comparison of Mars GCM dust storm simulations with Viking mission observations, 1999.

[34] Wilson, R. J., and M. I. Richardson, The Martian atmosphere during the Viking mission, I – Infrared measurements of atmospheric temperatures revisited, *Icarus*, *145*, 555–579, 2000.

[35] Zurek, R. W., Inference of dust opacities for the 1977 Martian great dust storms from Viking Lander 1 pressure data, *Icarus*, *45*, 202–215, 1981.

[36] Zurek, R. W., and L. J. Martin, Interannual variability of planet-encircling dust activity on Mars, *J. Geophys. Res.*, *98*, 3247–3259, 1993.